Supplemental Figures and Table

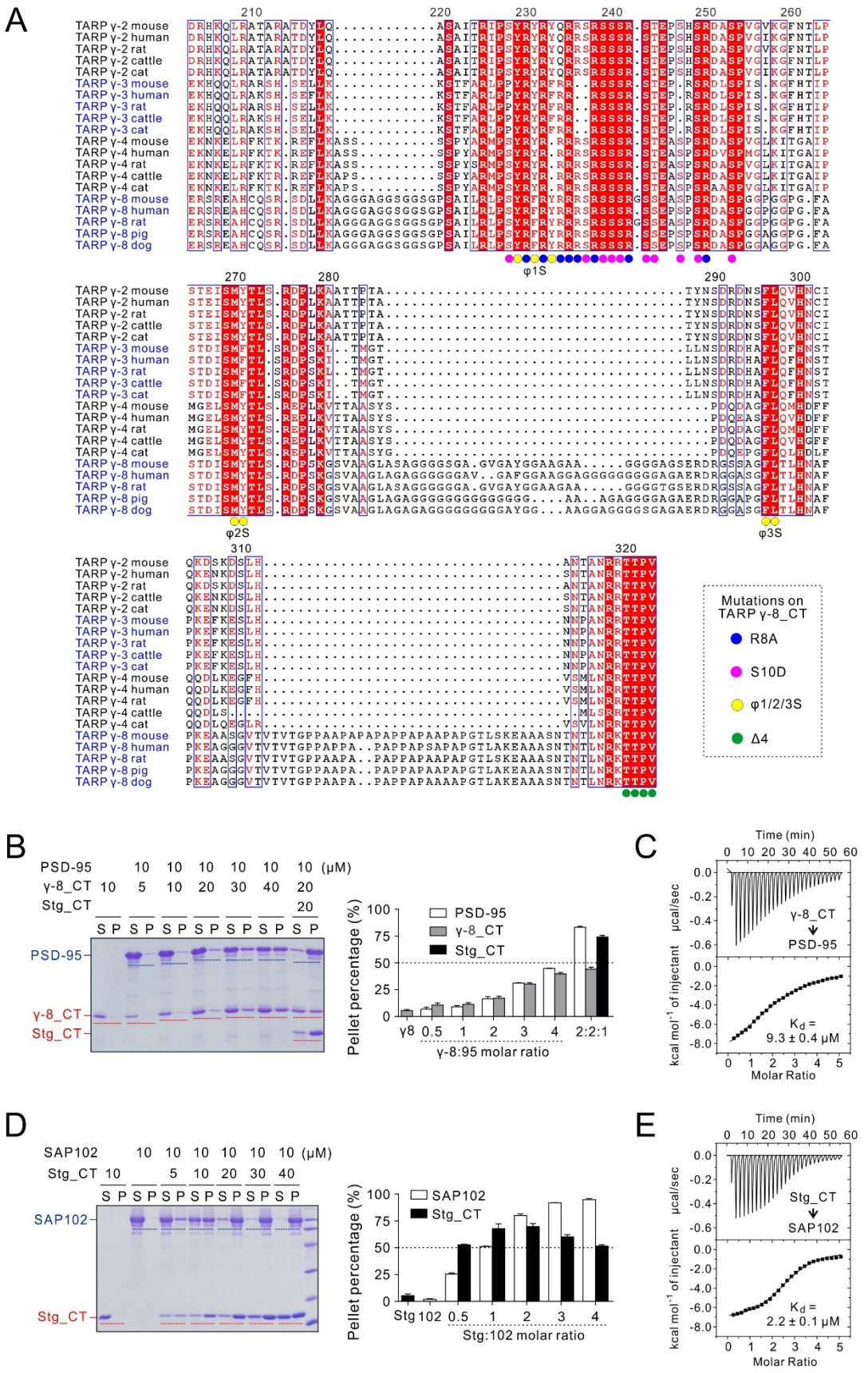
A
TARP γ-2 mouse
TARP γ-2 human
TARP γ-2 rat
TARP γ-2 cattle
TARP γ-2 cat
TARP γ-3 mouse
TARP γ-3 human
TARP γ-3 rat
TARP γ-3 cattle
TARP γ-3 cat
TARP γ-4 mouse
TARP γ-4 human
TARP γ-4 rat
TARP γ-4 cattle
TARP γ-4 cat
TARP γ-8 mouse
TARP γ-8 human
TARP γ-8 rat
TARP γ-8 pig
TARP γ-8 dog
φ1S
φ2S
φ3S
Mutations on TARP γ-8_CT
R8A
S10D
φ1/2/3S
Δ4
B
PSD-95
γ-8_CT
Stg_CT
S P
Pellet percentage (%)
γ-8:95 molar ratio
C
Time (min)
γ-8_CT
PSD-95
μcal/sec
kcal mol-1 of injectant
Kd = 9.3 ± 0.4 μM
Molar Ratio
D
SAP102
Stg_CT
Stg:102 molar ratio
E
Stg_CT
SAP102
Kd = 2.2 ± 0.1 μM

Supplemental Figure 1: Other TARP and MAGUK complexes also undergo LLPS. (Related to Figures 1&2)

A: Detailed sequence alignment of the cytoplasmic tails of TARP family members from different species. Totally conserved residues are labeled by white text in red background. Highly conserved residues are labeled by red text. Stg is referred to as TARP γ-2 here. Residues mutated in TARP γ-8_CT in Figure 6 corresponding to mutations in Stg_CT in Figure 2C are denoted by colored circles as indicated.

B: Sedimentation experiments showing higher γ-8:95 molar ratio promoted LLPS of the mixtures. In the last group, 20 μM TARP γ-8_CT, 20 μM Stg_CT and 10 μM PSD-95 were mixed, showing all three components were enriched in the condensed droplets.

C: ITC-based assay measuring the binding affinity between TARP γ-8_CT and PSD-95. TARP γ-8_CT at 250 μM was titrated into PSD-95 at 10 μM.

D: Sedimentation experiments showing the distribution of Stg_CT and SAP102 in aqueous/condensed phases. The quantification results in panels B and D were from 3 independent batches of sedimentation experiments and represented as mean ± SD.

E: ITC-based assay measuring the binding affinity between Stg_CT and SAP102. Stg_CT at 250 μM was titrated into SAP102 at 10 μM.

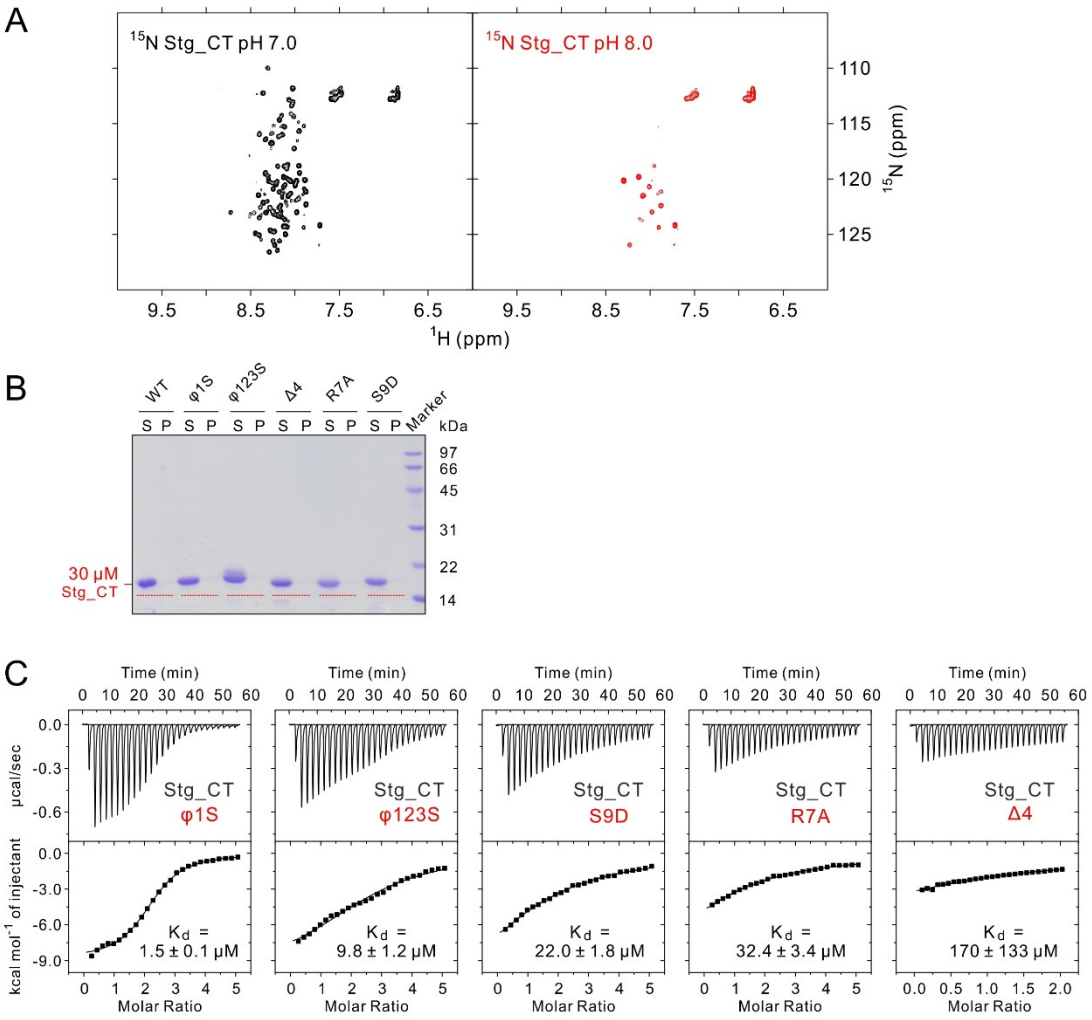

Supplemental Figure 2: Quality controls of Stg_CT in NMR, sedimentation experiments and ITC titrations. (Related to Figures 1-3)

A: ^{1}H, ^{15}N-HSQC spectra of the ^{15}N-labeled Stg_CT (0.1 mM) at pH 7.0 (left) and pH 8.0 (right). The narrow peak distributions of the spectra indicated that Stg_CT is intrinsically disordered, which is further confirmed by the overall peak disappearance upon raising the sample pH to 8.0.

B: Sedimentation experiments of 30 μM Stg_CT alone (WT or mutants) showing all mutant proteins were highly soluble and with high purity.

C: ITC-based measurement comparing the binding affinities of different Stg_CT (WT or mutants) to PSD-95. 250 μM PBM-containing mutant Stg_CT (φ1S, φ123S, S9D, R7A) was titrated into 10 μM PSD-95. 270 μM Stg_CT Δ4 without PBM was titrated into 27 μM PSD-95.

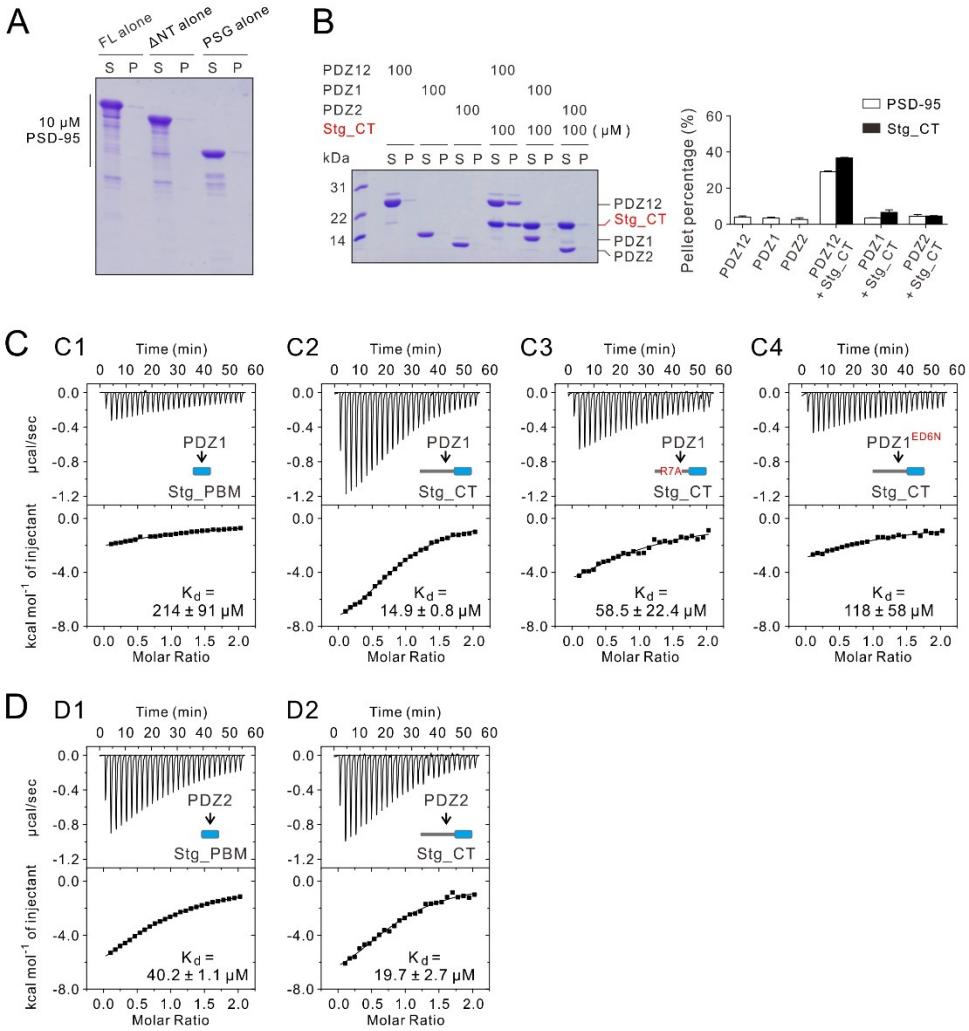

Supplemental Figure 3: Mechanisms of PSD-95 PDZ12 binding to Stg_CT. (Related to Figures 1-3)

A: Sedimentation experiments of 10 μM PSD-95 alone (WT or truncated fragments) showing the proteins were soluble and with good qualities.

B: Sedimentation experiments showing the mixtures of PSD-95 PDZ12 and Stg_CT underwent LLPS. 100 μM PSD-95 PDZ12, PDZ1 or PDZ2 alone were highly soluble. When mixed with 100 μM Stg_CT, PDZ12 & Stg_CT complex underwent LLPS while PDZ1 or 2 did not. Quantification results were from 3 independent batches of sedimentation experiments and represented as mean ± SD.

C: ITC-based measurements comparing the binding affinities between PSD-95 PDZ1 and Stg_PBM or Stg_CT. 500 μM PSD-95 PDZ1 was titrated into 50 μM Stg_PBM or Stg_CT as labeled.

D: ITC-based measurements comparing the binding affinities between PSD-95 PDZ2 and Stg_PBM or Stg_CT. 500 μM PSD-95 PDZ2 was titrated into 50 μM Stg_PBM or Stg_CT as labeled.

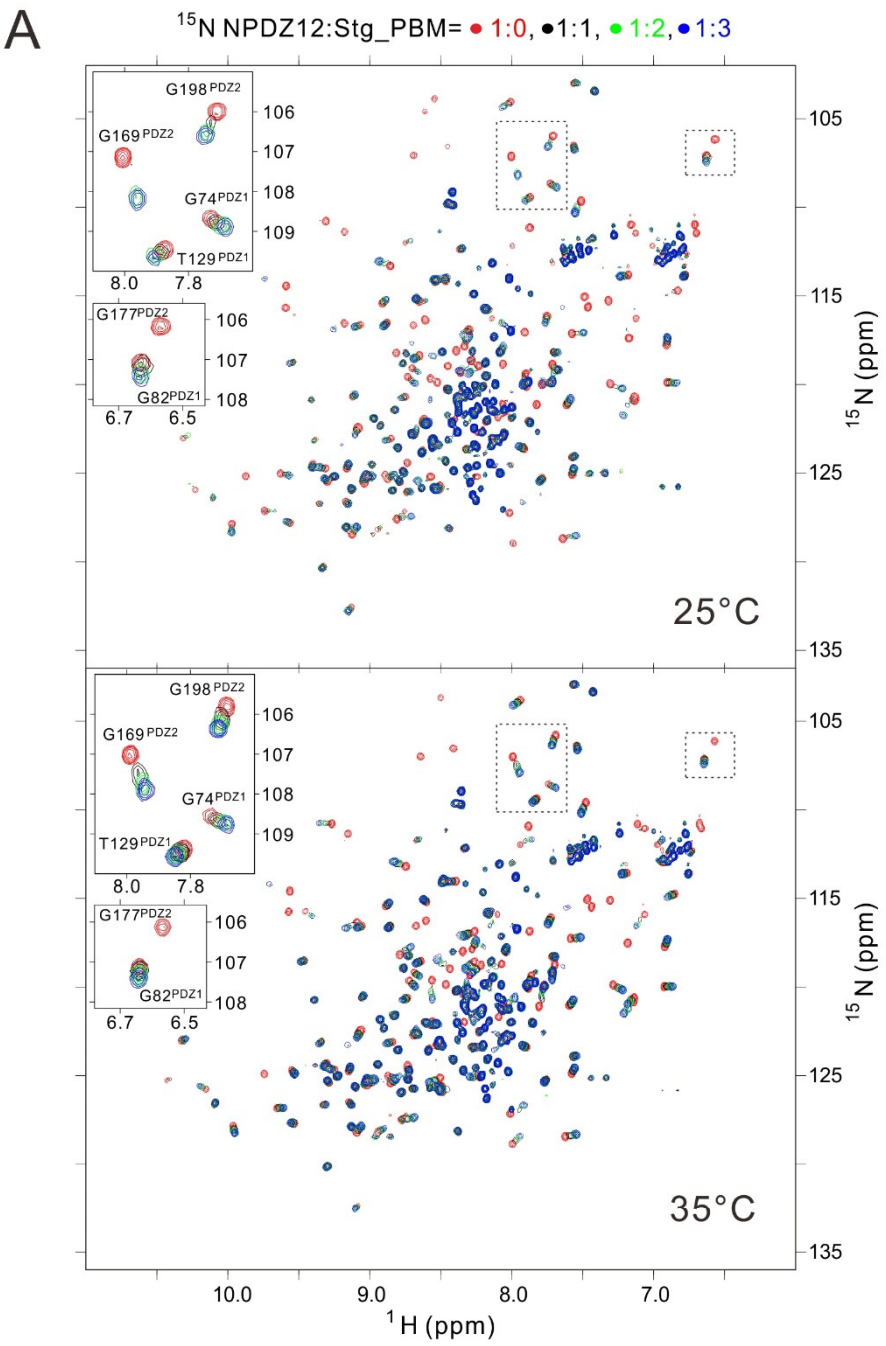
A
15N NPDZ12:Stg_PBM= ● 1:0, ●1:1, ● 1:2, ● 1:3
G198PDZ2
G169PDZ2
G74PDZ1
T129PDZ1
G177PDZ2
G82PDZ1
25°C
35°C
15N (ppm)
1H (ppm)
B
αA
βA
βF
βC
βD
βB
αB
180°
I143
F119
Y147
L118
Y63
F95
M149
M61
>30%
20-30%
10-20%
<10%
Residual peak intensity (%)

Supplemental Figure 4: NMR analysis of the Stg_CT binding sites on PSD-95 NPDZ12. (Related to Figure 3)

A: Superposition plot of the ^{1}H, ^{15}N-HSQC spectra of apo-form PSD-95 NPDZ12 (0.1 mM) (red), bound to Stg_PBM in 1:1 (black), 1:2 (green) and 1:3 (blue) molar ratios at 25°C (up) or 35°C (below). Insertions are zoom-in analyses of selected regions (dashed boxes) showing residues from PDZ1 or 2 underwent fast-intermediate exchanges at 25°C (up). When the sample temperature was raised to 35°C (below), the equilibrium shifted to fast exchange regime. It is noted that PDZ2 exhibited much more obvious chemical shift changes than PDZ1, suggesting a stronger interaction to Stg_PBM. The dashed box containing G82 and G177 is also shown in Figure 3D.

B: The residues in the PBM binding pocket of PSD-95 PDZ1 have minimal Stg_CT_Δ4 binding-induced chemical shift changes. Instead, the surface opposite to the PBM binding groove has large Stg_CT_Δ4 binding-induced shift changes as shown in Figure 3G. Backbone amide peak broadening of PDZ1 resulted from Stg_CT_Δ4 interaction was mapped to the structure of PDZ1 (PDB 2KA9). Ribbon combined the stick model showing the hydrophobic residues in negatively charged PDZ1 surface. The hydrophobic residues specifically conserved in PDZ1 (as indicated by green triangles in Figure 4H) are shown in bold-face letters.

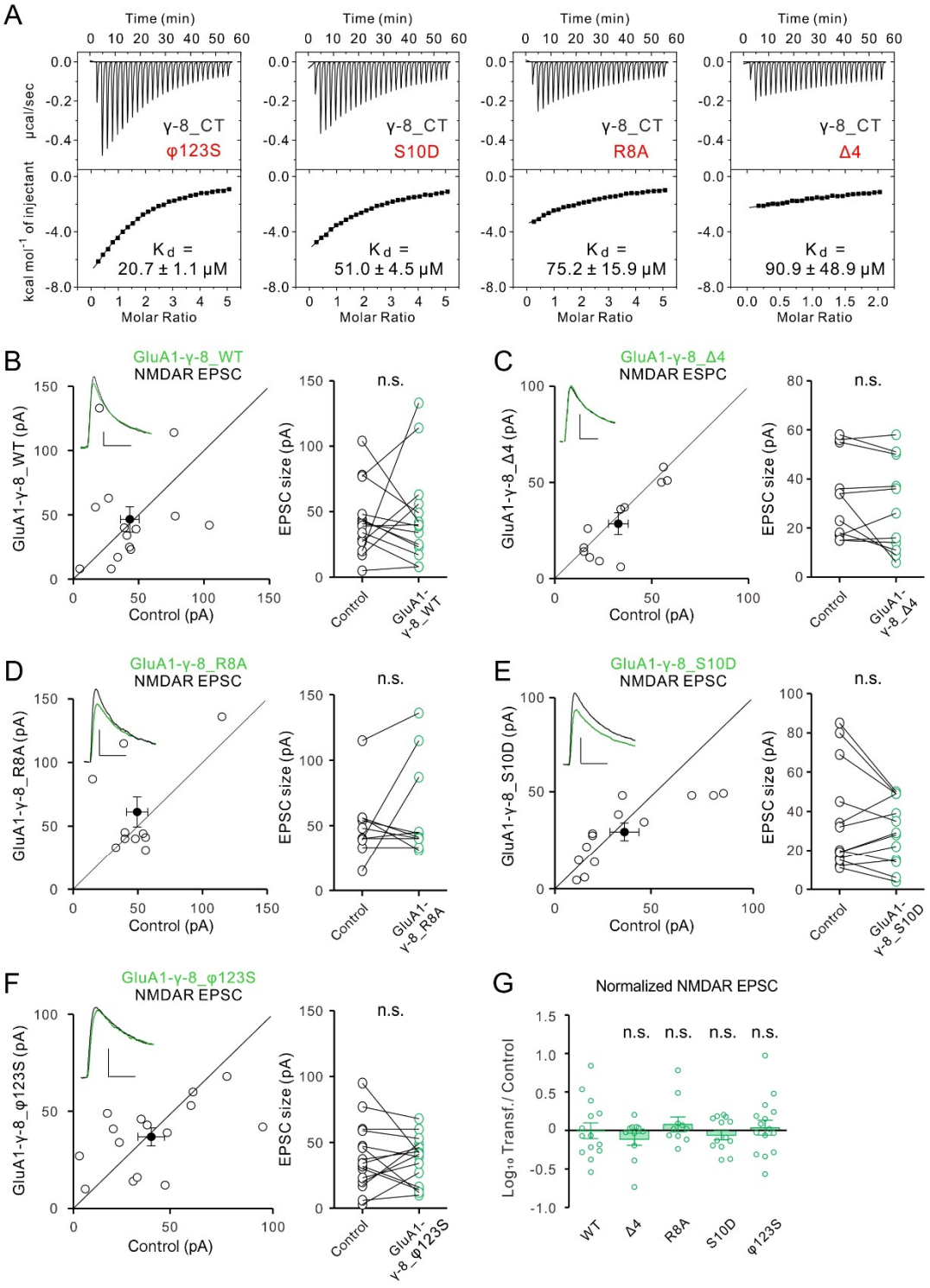

Supplemental Figure 5: Intact NMDAR EPSC upon endogenous AMPAR replacement with tethered GluA1-γ-8. (Related to Figure 6)

A: ITC-based measurements comparing the binding affinities between PSD-95 and different forms of TARP γ-8_CT. 250 μM PBM-containing mutant γ-8_CT (φ123S, S10D, R8A) was titrated into 10 μM PSD-95. 250 μM γ-8_CT Δ4 without PBM was

titrated into 25 μM PSD-95.

B-F: Scatterplots of NMDAR EPSC for single pairs (open circles) of control and GluA1-γ-8_WT (B, n = 14 pairs), GluA1-γ-8_Δ4 (C, n = 11 pairs), GluA1-γ-8_R8A (D, n = 10 pairs), GluA1-γ-8_S10D (E, n= 13 pairs) or GluA1-γ-8_φ123S (F, n = 15 pairs). Filled circles represent mean ± SEM. Insets show sample current traces from control (black) and transfected (green) neurons. Scale bars: 50 pA, 50 ms.

G: Summary plot comparing the log10 of the transfected/control neuron NMDAR EPSC ratio in all conditions tested. Statistical significance was analyzed using the Wilcoxon signed-rank test in B-F. One way ANOVA with Bonferroni multiple comparison test was used to compare relevant groups in G. n.s. not significant.

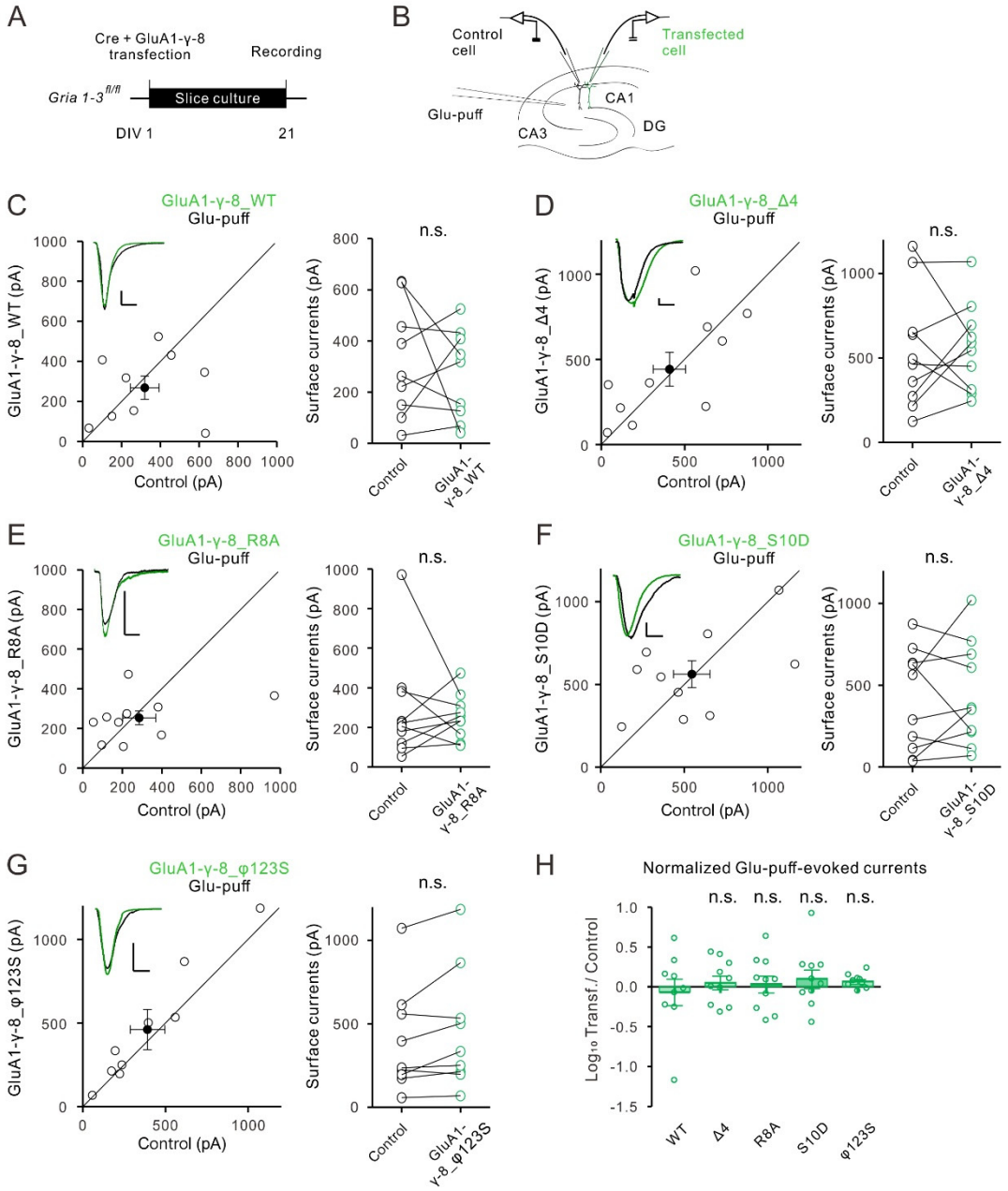

Supplemental Figure 6: Surface AMPAR currents upon endogenous AMPAR replacement with tethered GluA1-γ-8. (Related to Figure 6)

A: Timeline of the experiment.

B: Scheme of the AMPAR replacement strategy and dual whole-cell recordings from transfected (green) and control (black) CA1 pyramidal neurons. Surface currents are evoked by fast application of 1 mM glutamate.

C-G: Scatterplots (left) and paired dot plots (right) of surface currents evoked by fast application of 1 mM glutamate for single pairs (open circles) of control and GluA1-γ-8_WT. (C, n = 9 pairs), GluA1-γ-8_Δ4 (D, n = 10 pairs), GluA1-γ-8_R8A (E, n = 9 pairs), GluA1-γ-8_S10D (F, n = 10 pairs) or GluA1-γ-8_φ123S (G, n= 9 pairs). Filled circles represent mean ± SEM. Insets show sample current traces from control

(black) and transfected (green) neurons.

H: Summary plot comparing the $\log_{10}$ of the transfected/control neuron AMPAR surface current ratio in all conditions tested. Scale bars: 100 pA, 2 sec. Statistical significance was analyzed using the Wilcoxon signed-rank test in C-G. One way ANOVA with Bonferroni multiple comparison test was used to compare relevant groups in H.

Supplemental Table 1: Summary parameters for the ITC experiments described in the manuscript. (Related to Figures 1-3)

	Protein in syringe	Protein in cell	K_d (μM)	N value (sites)	ΔS (cal/mol/deg)
Figure 1B left	TRX-Stg_PBM	95_FL	48.5 ± 5.9	0.97 ± 0.36	-72.7
Figure 1B right	Stg_CT	95_FL	0.63 ± 0.06	2.21 ± 0.02	-5.1
Figure S1C	γ-8_CT	95_FL	9.3 ± 0.4	2.12 ± 0.03	-14.9
Figure S1E	Stg_CT	102_FL	2.2 ± 0.1	2.68 ± 0.02	1.2
Figure S2C	Stg_CT_φ1S	95_FL	1.5 ± 0.1	2.24 ± 0.02	-3.0
	Stg_CT_φ123S	95_FL	9.8 ± 1.2	2.71 ± 0.08	-10.8
	Stg_CT_S9D	95_FL	22.0 ± 1.8	1.69 ± 0.12	-30.7
	Stg_CT_R7A	95_FL	32.4 ± 3.4	1.11 ± 0.22	-41.0
	Stg_CT_Δ4	95_FL	170 ± 133	N.R	N.R
Figure S3C	95_PDZ1	TRX-Stg_PBM	214 ± 91	N.R	N.R
	95_PDZ1	Stg_CT	14.9 ± 0.8	0.92 ± 0.01	-9.8
	95_PDZ1	Stg_CT_R7A	58.5 ± 22.4	0.99 ± 0.23	-12.9
	95_PDZ1_ED6N	Stg_CT	118 ± 58	N.R	N.R
Figure S3D	95_PDZ2	TRX-Stg_PBM	40.2 ± 1.1	0.87 ± 0.01	-15.9
	95_PDZ2	Stg_CT	19.7 ± 2.7	0.89 ± 0.04	-8.6
Figure S5A	γ-8_CT_φ123S	95_FL	20.7 ± 1.1	1.02 ± 0.08	-47.4
	γ-8_CT_S10D	95_FL	51.0 ± 4.5	N.R	N.R
	γ-8_CT_R8A	95_FL	75.2 ± 15.9	N.R	N.R
	γ-8_CT_Δ4	95_FL	90.9 ± 48.9	N.R	N.R

N.R: no reliable data could be obtained due to very weak binding